Observation of Perfectly-Chiral Exceptional Point via Bound State in the Continuum

Zhiling Zhou[*], Bin Jia,[*] Nengyin Wang, Xu Wang,[†] and Yong Li[‡]

Institute of Acoustics, Tongji University, Shanghai 200092, China

Chirality is one of the fundamentals of nature with strong ties to asymmetry. In wave physics, it is conventionally characterized by asymmetric scattering of circularly polarized waves but suffers from two-state polarization. To overcome the limitation, here we demonstrate the concept of extreme chirality regarding orbital angular momentum (OAM) helicity, originating from a chiral quasibound state in the continuum held by a mirror-symmetry-broken metasurface. Empowered by the intrinsic OAM-selective coupling nature of the metasurface, the system arrives at a peculiar state where the left-handed incident vortex is completely absorbed while the right-handed counterpart is totally reflected, namely, a perfectly-chiral exceptional point. The realization of asymmetric OAM modulation creates the possibility to explore chirality with unlimited states. Our work raises a new paradigm for the study of extreme OAM chirality and enriches the physics of chiral wave-matter interaction.

Chirality is one of the fundamentals of nature with strong ties to asymmetric phenomena ranging from microscopic to macroscopic scale [1–3]. In wave physics, chirality is conventionally characterized by the system's scattering features, typically the asymmetric response to circularly polarized (CP) waves with opposite polarization helicity. Weak chiral effects such as circular dichroism commonly exist in masses of symmetry-broken natural matters. But it is challenging to enlarge these effects to an extreme level [4–7] with the dominating physics indistinct.

Recently, the exploration of achiral asymmetric behavior of non-Hermitian systems at exceptional points (EPs) has given novel understanding to this topic [8–12]. With judiciously tailored gain and/or loss, extreme achiral phenomena such as unidirectional invisibility [13–15], directional lasing [16], and extremely asymmetric absorption or reflection [17–19] have been observed in $\mathcal{PT}$-symmetric systems and other passive systems [20–22].

To date, although maximally asymmetric transmission and maximized circular dichroism of CP light have been realized [23–25], chirality in this scenario is confined to the two-state spin angular momentum from circular polarization. In contrast, orbital angular momentum (OAM) can be arbitrarily manipulated to create unlimited states encoding multiple chiral information [26–30], which provides broader horizons for the exploration of fruitful physics of chirality [31–33].

In this Letter, we theoretically and experimentally elaborate on the concept of extreme chirality via asymmetric scattering of vortex waves carrying opposite OAM in the non-Hermitian system at a perfectly-chiral EP. Generally, a scattering EP only suggests the vanishment of abnormal reflection regarding one OAM helicity. We further, remarkably, maximize the other abnormal reflection for the opposite helicity. Such a so-called perfectly-chiral EP is induced by a quasibound state in the continuum (QBIC) [34–37] featuring weak yet extremely chiral radiation. These concepts are demonstrated via a mirror-symmetry-broken metasurface mounted in a cylindrical waveguide, serving as the breeding ground for the EP. Here, we showcase the theoretical ground and proof-of-principle experiments in acoustics. Empowered by the QBIC's OAM-helicity sensitivity originating from the chiral radiation, the non-Hermitian system arrives at the perfectly-chiral EP supporting extreme chirality, which is manifested by complete absorption of the left-handed incident vortex and total reflection of the right-handed counterpart.

The general picture of OAM chirality at perfectly-chiral EP is depicted by the interplay between external excitations with opposite OAM helicity states ($|\pm\rangle$) and a QBIC held by the metasurface mounted at the end of a waveguide (Fig. 1). The circular symmetry of the waveguide engenders orthogonal vortex mode pairs with opposite handedness, which can be expressed as $p_{(m,n)}=A_{m,n}J_m(k_{m,n}r)e^{\pm jk_zz}e^{jm\theta}$, where $A_{m,n}$ is the mode amplitude, J_m is the mth-order Bessel function, $k_{m,n}$ is the transverse eigen-wave-number, $k_z = \sqrt{k_0^2 - k_{m,n}^2}$ is the axial wave number, and $m = 0, \pm 1, \ldots, \pm\infty$ is the topological charge representing OAM of different order. The circular metasurface placed at the bottom of the waveguide serves as a scatterer. Particularly, symmetries of the metasurface intrinsically capture the pattern of scattered fields. The rotational symmetry governs the conservation of the topological charges of scattered modes, which is summarized into [32,38]

$$m_{\mathrm{re}} = m_{\mathrm{in}} + sT, \tag{1}$$
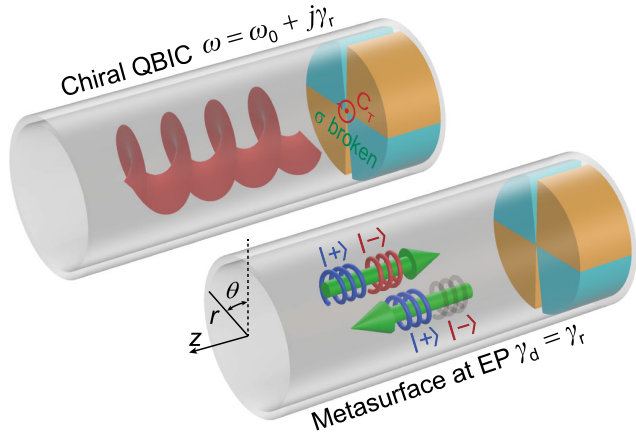
FIG. 1. Schematics of extreme OAM chirality at the perfectly-chiral EP. Upper panel: a chiral QBIC held by the metasurface featuring weak yet extremely chiral radiation at the eigenfrequency $\omega = \omega_0 + j\gamma_r$. Lower panel: extremely asymmetric scattering response at the perfectly-chiral EP in the critical coupling regime ($\gamma_d = \gamma_r$).

where m_{in} and m_{re} are the topological charge of incident and reflected vortex, respectively, $s = 0, \pm 1, \ldots, \pm\infty$ is the diffraction order, and T is the group number of the subunits relating to the Tth-order rotational symmetry with respect to the z axis (C_T symmetry group). On the other side, breaking the mirror symmetry plays a key role in the emergence of chirality, giving access to a unique QBIC exhibiting extremely chiral radiation field. This intrinsic property further engenders a perfectly-chiral scattering EP associated with extreme OAM chirality when the dissipative decay rate (γ_d) balances the radiative decay rate (γ_r) of the excited QBIC, i.e., $\gamma_r = \gamma_d$.

To demonstrate the physics neatly and concisely, the OAM takes first order as an illustration. Hence, the frequency band of concern is confined to a range where all modes are excluded except for $p_{(0,0)}$, $p_{(-1,0)}$, and $p_{(+1,0)}$. In particular, the achiral mode $p_{(0,0)}$ carrying zero OAM is undesirable in the exploration of chirality. One can eliminate this impact by preserving the metasurface's rotational symmetry. According to Eq. (1), when the C_2 symmetry is preserved ($T = 2$) and the incident waves take $m_{\mathrm{in}} = \pm 1$, the scattered field consists only of chiral modes $p_{(-1,0)}$ and $p_{(+1,0)}$. Therefore, now the left- ($|-\rangle$) and right-handed ($|+\rangle$) OAM states are specifically represented by the $p_{(-1,0)}$ and $p_{(+1,0)}$ mode.

Mathematically, scattering behavior of such a two-port system can be described by the S-matrix equation:

$$\begin{pmatrix} A_-^{\mathrm{re}} \\ A_+^{\mathrm{re}} \end{pmatrix} = \begin{pmatrix} r_{--} & r_{+-} \\ r_{-+} & r_{++} \end{pmatrix} \begin{pmatrix} A_-^{\mathrm{in}} \\ A_+^{\mathrm{in}} \end{pmatrix}, \qquad (2)$$

where $A_\pm^{\mathrm{in}}$ and $A_\pm^{\mathrm{re}}$ are the incident and reflected mode amplitudes, respectively, with the subscript referring to $|\pm\rangle$

states and the superscript indicating incidence and reflection. Specular reflections from both channels are identical owing to the reciprocity, i.e., $r_{--} = r_{++}$. Therefore, chirality of the system stems from the difference between r_{+-} and r_{-+}.

A metasurface with the primitive cell consisting of two fanlike grooves with different span angles (θ_1, θ_2) and depths (L_1, L_2) is constructed. Two identical counterparts are obtained by performing 180° rotational operation to the primitive cell with respect to the metasurface's axis. This configuration ensures the C_2 rotational symmetry and mirror symmetry with respect to two planes noted as σ_1 and σ_2 [Fig. 2(a)]. The coupling strength is described by the imaginary part of the complex eigenfrequency $\omega = \omega_0 + j\gamma_r$, where ω_0 and γ_r are the resonance frequency and radiative decay rate, respectively. Then the radiative quality factor can be derived from $Q_r = \omega_0/(2\gamma_r)$. Starting from structural parameters $\theta_1 = 110°$, $\theta_2 = 50°$, $\theta_0 = 10°$, $L_1 = 48.63$ mm, $R_e = 48$ mm, and $R_i = 16$ mm, eigenfrequency analysis is performed by COMSOL MULTIPHYSICS (see Supplemental Material, Sec. B [39]). For the emergence of chirality, perturbation in span angle ($\Delta\theta$) and depth (L_2') of groove 2 are continuously varied [Fig. 2(b)], defining the parameter space $\Gamma = (\Delta\theta, L_2')$. We note that these two parameters are closely related to the evolution of two eigenstates (see Supplemental Material, Sec. C for details [39]). It is found that the radiative quality factor Q_r exceeds 10^6 at $\Delta\theta = 0°$ and $L_2' = 18.1$ mm, where the eigenstate possesses a purely real eigenfrequency $\omega_{\mathrm{BIC}} = 2\pi \times 3136.3$ Hz [Fig. 2(c)]. This divergent point symbolizes a perfect bound state embedded in the continuum (BIC) spanned by the propagating vortices [37,40]. Around the BIC, the eigenstates with finite Q_r are QBICs which couple to the continuum and essentially affect the scattering features of the metasurface.

Via circumferential mode decomposition method (see Supplemental Material, Sec. D [39]), we decompose the radiation field of the QBICs. The proportion of mode $|-\rangle$, represented by the relative amplitude, is shown in Fig. 2(d). As observed, the parameter space is segmented into four regions by the dashed lines, where the OAM is counteracted by the equal $|-\rangle$ and $|+\rangle$ and hence indicating achiral QBICs. These lines intersect at the BIC (star), which serves as a singularity of chirality in the parameter space where the OAM helicity is undefined. Within each region, unequal-proportion modes $|-\rangle$ and $|+\rangle$ coexist in the radiation field because of the broken mirror symmetry, inducing clockwise (CW) or counterclockwise OAM represented by the intensity flux.

We note that a unique QBIC, named chiral QBIC, emerges when one of the two modes vanishes in the radiation field. Here, the selected QBIC [red dot in Fig. 2(d)] with $\omega_c = 2\pi \times (3117.4 + 5.6657j)$ Hz exhibits over 99.9% of mode $|-\rangle$. To unfold more details, the real part of sound pressure and intensity flux distribution of this
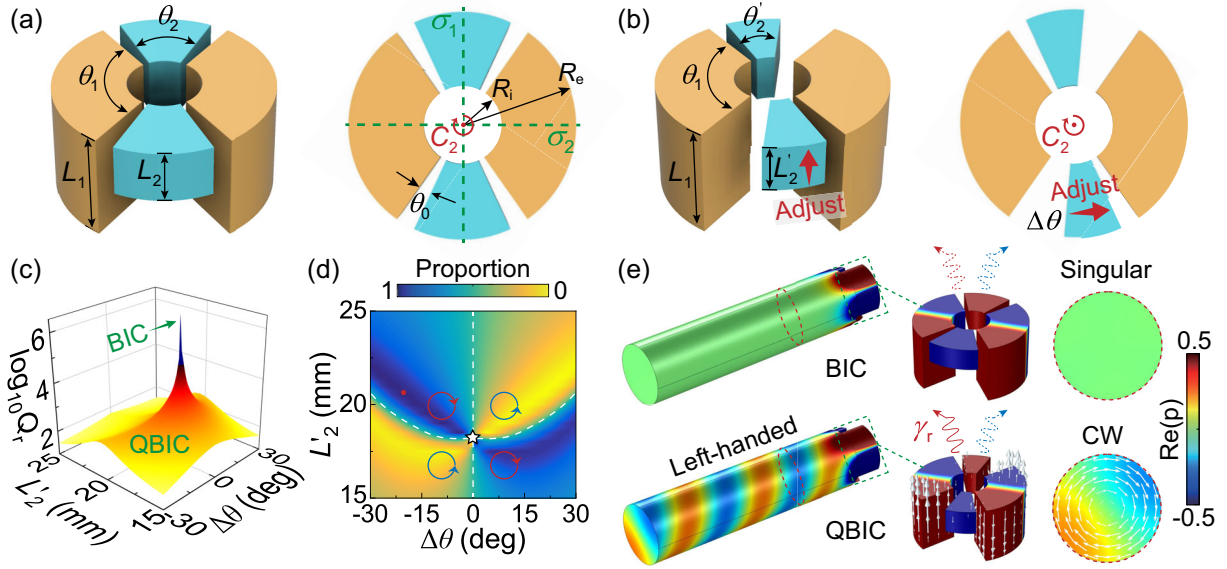
FIG. 2. (a) Left: schematic of metasurface with C_2 rotational symmetry and $\sigma_{1,2}$ mirror symmetry. θ_0 is the span angle of the wall. R_i and R_e are the inner and external radius, respectively. Right: cross section of the metasurface. (b) Left: schematic of the chiral metasurface. Right: cross section. $\Delta\theta$ denotes the perturbation of span angle of groove 2. Note that (a) and (b) depict the air domains bounded by the fanlike grooves. (c) Radiative quality factor of eigenstates held by the metasurface. (d) Proportion of mode $|-\rangle$ in the radiation field. The dashed lines indicate achiral QBICs with equal $|+\rangle$ and $|-\rangle$. The circles with arrows denote the helicity of OAM in radiation field. The star and red dot respectively mark the BIC and the selected chiral QBIC. (e) Real part of sound pressure p and intensity distribution from the radiation field of BIC (upper panel) and the chiral QBIC (lower panel). See detailed geometrical parameters in Supplemental Material, Sec. A [39].

QBIC are compared with that of BIC [Fig. 2(e)]. As observed, the BIC exhibits zero radiation in both channels. Whereas, the QBIC with CW OAM, distinguishingly, radiates exclusively toward the left-handed channel, drawing a spiral radiation field. As shown later, such selective radiation from the chiral QBIC will trigger the extreme asymmetrical response of the metasurface.

According to the coupled mode theory (see Supplemental Material, Sec. E [39]), an eigenstate's coupling to the continuum turns into eigenradiation from the view of time reversal. The coupling strength is directly determined by its radiative decay rate (imaginary part of ω): $|u_-|^2 + |u_+|^2 = 2\gamma_r$, where $u_\pm$ describe the coupling strength in left- and right-handed channels. From this perspective, the selective radiation of chiral QBIC in Fig. 2(e) results from $u_+ = 0$, indicating a full decouple to the continuum in right-handed channel.

Consider that the intrinsic dissipation breaks the system's Hermiticity and engenders asymmetric scattering. One essential manifestation is the difference in the absorption rate of incident vortices. For the mentioned chiral QBIC at resonance frequency, $|u_+|^2 = 0$ and $|u_-|^2 = 2\gamma_r$ yield $\alpha_- - \alpha_+ = 8\gamma_d|u_-|^2/(2\gamma_d + |u_-|^2)^2$, where γ_d is the dissipative decay rate and $\alpha_\pm$ is the absorption rate of the corresponding incident vortex. When $|u_-|^2 = 2\gamma_d$ is also guaranteed, the absorption difference reaches a maximum with $\alpha_- = 1$ and $\alpha_+ = 0$. These conditions lead to $\gamma_d = \gamma_r$, indicating the critical coupling regime. Therefore, given

that the chiral QBIC imparts γ_r matching γ_d while it remains decoupled to the right-handed channel, the metasurface will exhibit extreme chirality.

Mode matching theory is developed to solve the scattered fields (see Supplemental Material, Sec. F [39]). Neglecting the intrinsic loss, uniqueness of the chiral QBIC can be understood from the average acoustic energy density in the grooves of the metasurface [Fig. 3(a)]. For incident vortex $|+\rangle$ with an amplitude of 2 Pa at 3112 Hz, eigenmodes in the grooves remain weakly activated and the average energy density maintains at a low level of 7.5×10^{-6} J/m³. With the handedness of the incidence flipped, in stark contrast, the modes corresponding to the profile of QBIC in Fig. 2(e) are strongly excited and dominate the grooves, boosting the average energy density to 1×10^{-3} J/m³ (see Supplemental Material, Sec. F [39]). The significantly enhanced average energy density (more than 122 times) demonstrates the pronounced wave-matter interaction originating from excitation of the chiral QBIC. Such chiral excitation is evidence of the QBIC's selective coupling to the OAM helicity carried by incident vortices.

According to the effective medium theory, the intrinsic loss can be introduced as an imaginary part of the complex sound speed in the grooves ($c = c_r + jc_i$), then reflectivity spectra in Eq. (2) is calculated. For the selected parameters corresponding to the QBIC [Fig. 2(e)], the critical coupling condition is met at the resonance frequency (3112 Hz) when $c = 343 \times (1 + 0.0021j)$ m/s (see Supplemental
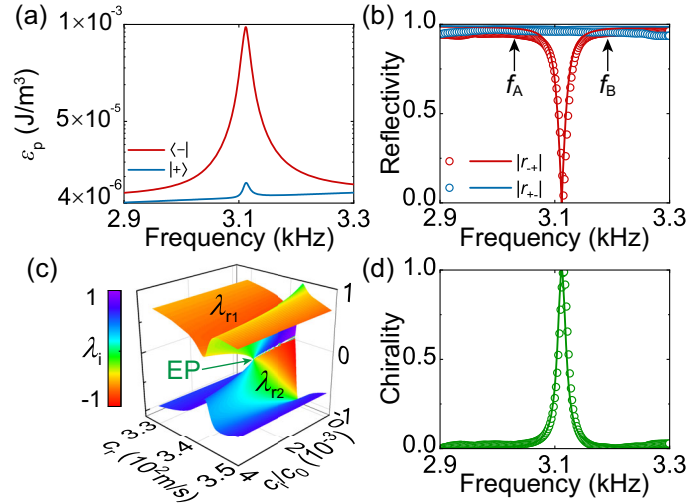
FIG. 3.   (a) Theoretical average acoustic energy density (ε_p) in the metasurface excited by $|-\rangle$ (red line) and $|+\rangle$ (blue line) vortex. (b) Theoretical (solid lines) and experimental (circles) reflectivity spectra. (c) Riemann surfaces of the complex eigenvalues of the S matrix versus real (c_r) and imaginary part (c_i) of the complex sound speed. The real and imaginary parts of the eigenvalues are quantified by the vertical axis and the color bar, respectively. (d) Theoretical (line) and experimental (circles) chirality.

Material, Sec. G [39]). Because of the high Q_r resonance, the tiny loss substantially affects the reflectivity, leading to an extreme difference between $|r_{-+}|$ and $|r_{+-}|$ [Fig. 3(b)]. Whereas, the normal reflection terms, $|r_{++}|$ and $|r_{--}|$, remain comparatively low (see Supplemental Material, Sec. H). Theoretical prediction shows that $|r_{-+}|$ reduces to zero at 3112 Hz, and $|r_{+-}|$ steadily retains over 99% in the whole spectrum. The experimental point around the EP is observed with the minimum value $|r_{-+}| = 0.041$ and maximum value $|r_{+-}| = 0.96$. Interestingly, away from the

resonance where the frequency $f < f_A$ or $f > f_B$, $|r_{-+}|$ approximates $|r_{+-}|$ in broadband and the S matrix reduces to a Hermitian form [Fig. 3(c)]. This spectral-sensitive feature implies that the intrinsic loss is negligible, and the system behaves Hermitian until the QBIC is excited.

At 3112 Hz, Riemann surface of the complex eigenvalues ($\lambda_{1,2} = r_{--} \pm \sqrt{r_{-+}r_{+-}}$) of the S matrix are obtained with the real and imaginary part of the complex sound speed varying [Fig. 3(c)]. It is observed that the system arrives at EP when the critical coupling condition is met
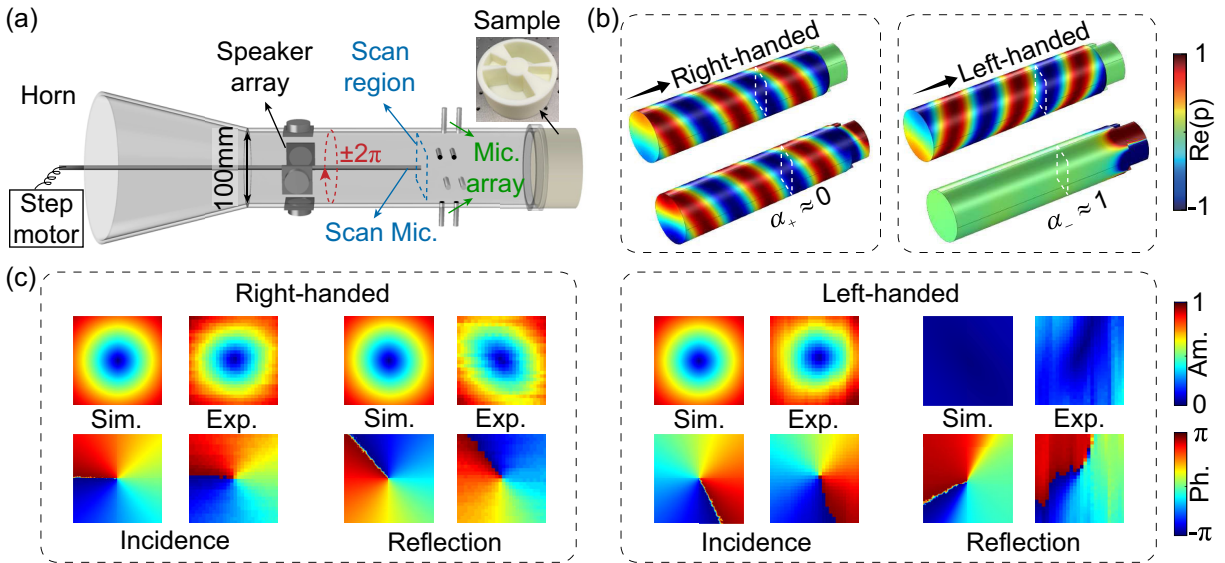
FIG. 4.   (a) Schematic of the experiment platform. The scan microphone connected to a motor moves in a step of 1 mm within the blue region. (b) Simulated incident and reflected distribution of real part of sound pressure p. (c) Experimental scanning results against simulated results of incidence and reflected fields at 150 mm above the metasurface [cross section encircled by the dashed line in (b)]. The upper and lower rows respectively present the amplitude and phase distribution.

with $c = 343 \times (1 + 0.0021j)$ m/s. At this very point, the vanishment of one abnormal reflection term ($|r_{-+}| \approx 0$) renders the system's S matrix reduced to a Jordan form, accompanied by simultaneous collapse of its eigenvalues and eigenvectors, which can be universally observed at EPs. What should be noted here is that the other abnormal reflection term can approach unity resulting from the decoupling to excitation ($|r_{+-}| \approx 1$). This so-called perfectly-chiral EP enables the chirality defined as chirality $= ||r_{+-}|^2 - |r_{-+}|^2|/||r_{+-}|^2 + |r_{-+}|^2|$ to approach unity at the resonance frequency [Fig. 3(d)]. The extreme chirality, empowered by the encoded chiral QBIC, makes our design stand in stark contrast to previously proposed chiral metasurface. It should be pointed out that the observation of BIC and perfectly-chiral EP is based on two representations of the scattering system. The perfectly-chiral EP is realized from the S matrix by leveraging the (Q) BIC found in the effective Hamiltonian, the H matrix (see Supplemental Material, Sec. I [39]).

A series of experiments have been performed on the demonstration platform [Fig. 4(a)] (see the details in Supplemental Material, Sec. J [39]). Based on extensive experimental investigation, we capture the scattering behavior around the BIC (Fig. S9 of Supplemental Material) and the perfectly-chiral EP [Fig. 3(c)]. Excellent agreement between the theoretical and experimental results provides solid proof for the accuracy of our work. The scattering features at the EP are of particular interest. Figure 4(b) shows the simulated incident and reflected field of the real part of sound pressure p. For comparison, amplitude and phase distribution at the white region in Fig. 4(b) are replotted in Fig. 4(c). As observed, the scanned amplitude and phase distribution (constituted by a 25×25 pixel array obtained from a 50×50 mm^2 scan region with a scanning step of 2 mm) fit well with the simulated results. The above results reveal the extreme chirality of the metasurface at the perfectly-chiral EP, manifested by complete absorption of the left-handed incident vortex and total reflection of the right-handed counterparts.

In conclusion, our work theoretically and experimentally studies the intrinsic properties and scattering features of a spectral- and OAM-sensitive metasurface operating at the perfectly-chiral EP. It is demonstrated that extreme acoustical chirality is encoded in such a perfectly-chiral EP where the metasurface completely absorbs the left-handed incident vortex and totally reflects the right-handed counterpart. Since the methodology here is not limited by the OAM order, this attempt may open up promising opportunities for revealing plentiful chiral phenomena in multichannel vortex systems [41], which could inspire topics such as tunable vortex lasing [28], OAM-based communication [33], and higher-order OAM-chiral EP [42,43].

---

*These authors contributed equally to this work.
†xuwang@tongji.edu.cn
‡yongli@tongji.edu.cn

[1] V. Prelog, Science **193**, 17 (1976).
[2] M. Hentschel, M. Schaferling, X. Duan, H. Giessen, and N. Liu, Sci. Adv. **3**, e1602735 (2017).
[3] Y. Tang and A. E. Cohen, Phys. Rev. Lett. **104**, 163901 (2010).
[4] C. Chen, S. Gao, W. Song, H. Li, S. N. Zhu, and T. Li, Nano Lett. **21**, 1815 (2021).
[5] W. Chen, Q. Yang, Y. Chen, and W. Liu, Phys. Rev. Lett. **126**, 253901 (2021).
[6] V. A. Fedotov, P. L. Mladyonov, S. L. Prosvirnin, A. V. Rogacheva, Y. Chen, and N. I. Zheludev, Phys. Rev. Lett. **97**, 167401 (2006).
[7] M. Turduev, M. Botey, I. Giden, R. Herrero, H. Kurt, E. Ozbay, and K. Staliunas, Phys. Rev. A **91**, 023825 (2015).
[8] R. El-Ganainy, K. G. Makris, M. Khajavikhan, Z. H. Musslimani, S. Rotter, and D. N. Christodoulides, Nat. Phys. **14**, 11 (2018).
[9] M. A. Miri and A. Alu, Science **363**, eaar7709 (2019).
[10] S. K. Ozdemir, S. Rotter, F. Nori, and L. Yang, Nat. Mater. **18**, 783 (2019).
[11] H.-Z. Chen, T. Liu, H.-Y. Luan, R.-J. Liu, X.-Y. Wang, X.-F. Zhu, Y.-B. Li, Z.-M. Gu, S.-J. Liang, H. Gao, L. Lu, L. Ge, S. Zhang, J. Zhu, and R.-M. Ma, Nat. Phys. **16**, 571 (2020).
[12] C. Q. Wang, W. R. Sweeney, A. D. Stone, and L. Yang, Science **373**, 1261 (2021).
[13] Y. Huang, Y. Shen, C. Min, S. Fan, and G. Veronis, Nanophotonics **6**, 977 (2017).
[14] Z. Lin, H. Ramezani, T. Eichelkraut, T. Kottos, H. Cao, and D. N. Christodoulides, Phys. Rev. Lett. **106**, 213901 (2011).
[15] L. Feng, Y. L. Xu, W. S. Fegadolli, M. H. Lu, J. E. Oliveira, V. R. Almeida, Y. F. Chen, and A. Scherer, Nat. Mater. **12**, 108 (2013).
[16] B. Peng, S. K. Ozdemir, M. Liertzer, W. Chen, J. Kramer, H. Yilmaz, J. Wiersig, S. Rotter, and L. Yang, Proc. Natl. Acad. Sci. U.S.A. **113**, 6845 (2016).
[17] Q. Song, M. Odeh, J. Zuniga-Perez, B. Kante, and P. Genevet, Science **373**, 1133 (2021).
[18] W. R. Sweeney, C. W. Hsu, S. Rotter, and A. D. Stone, Phys. Rev. Lett. **122**, 093901 (2019).
[19] X. Wang, X. Fang, D. Mao, Y. Jing, and Y. Li, Phys. Rev. Lett. **123**, 214302 (2019).
[20] W. Zhu, X. Fang, D. Li, Y. Sun, Y. Li, Y. Jing, and H. Chen, Phys. Rev. Lett. **121**, 124501 (2018).
[21] C. M. Bender and S. Boettcher, Phys. Rev. Lett. **80**, 5243 (1998).
[22] X. Zhu, H. Ramezani, C. Shi, J. Zhu, and X. Zhang, Phys. Rev. X **4**, 031042 (2014).

[23] M. Kang, J. Chen, and Y. D. Chong, Phys. Rev. A **94,** 033834 (2016).

[24] M. V. Gorkunov, A. A. Antonov, and Y. S. Kivshar, Phys. Rev. Lett. **125,** 093903 (2020).

[25] A. V. Kondratov, M. V. Gorkunov, A. N. Darinskii, R. V. Gainutdinov, O. Y. Rogov, A. A. Ezhov, and V. V. Artemov, Phys. Rev. B **93,** 195418 (2016).

[26] L. Allen, M. W. Beijersbergen, R. J. C. Spreeuw, and J. P. Woerdman, Phys. Rev. A **45,** 8185 (1992).

[27] P. Miao, Z. Zhang, J. Sun, W. Walasik, S. Longhi, N. M. Litchinitser, and L. Feng, Science **353,** 464 (2016).

[28] Z. Zhang, X. Qiao, B. Midya, K. Liu, J. Sun, T. Wu, W. Liu, R. Agarwal, J. M. Jornet, S. Longhi, N. M. Litchinitser, and L. Feng, Science **368,** 760 (2020).

[29] J. Ni, C. Huang, L. M. Zhou, M. Gu, Q. Song, Y. Kivshar, and C. W. Qiu, Science **374,** eabj0039 (2021).

[30] A. T. O'Neil, I. MacVicar, L. Allen, and M. J. Padgett, Phys. Rev. Lett. **88,** 053601 (2002).

[31] B. Wang, W. Liu, M. Zhao, J. Wang, Y. Zhang, A. Chen, F. Guan, X. Liu, L. Shi, and J. Zi, Nat. Photonics **14,** 623 (2020).

[32] Y. Fu, C. Shen, X. Zhu, J. Li, Y. Liu, S. A. Cummer, and Y. Xu, Sci. Adv. **6,** eaba9876 (2020).

[33] J. Wang, J. Yang, I. Fazal, N. Ahmed, Y. Yan, H. Huang, Y. Ren, Y. Yue, S. Dolinar, M. Tur, and A. Willner, Nat. Photonics **6,** 488 (2012).

[34] K. Koshelev, S. Lepeshov, M. Liu, A. Bogdanov, and Y. Kivshar, Phys. Rev. Lett. **121,** 193903 (2018).

[35] A. Overvig, N. Yu, and A. Alu, Phys. Rev. Lett. **126,** 073001 (2021).

[36] A. A. Lyapina, D. N. Maksimov, A. S. Pilipchuk, and A. F. Sadreev, J. Fluid Mech. **780,** 370 (2015).

[37] C. W. Hsu, B. Zhen, A. D. Stone, J. D. Joannopoulos, and M. Soljačić, Nat. Rev. Mater. **1,** 16048 (2016).

[38] Y. Xie, W. Wang, H. Chen, A. Konneker, B. I. Popa, and S. A. Cummer, Nat. Commun. **5,** 5553 (2014).

[39] See Supplemental Material at http://link.aps.org/supplemental/10.1103/PhysRevLett.130.116101 for parameters of the meta-surface, details of simulations, discussions about the BICs, details of theoretical calculations, discussions about the Hamiltonian matrix and Scattering matrix, and details of experiments.

[40] H. Friedrich and D. Wintgen, Phys. Rev. A **32,** 3231 (1985).

[41] J. Ni, S. Liu, D. Wu, Z. Lao, Z. Wang, K. Huang, S. Ji, J. Li, Z. Huang, Q. Xiong, Y. Hu, J. Chu, and C. W. Qiu, Proc. Natl. Acad. Sci. U.S.A. **118,** e2020055118 (2021).

[42] X. Fang, N. Gerard, Z. Zhou, H. Ding, N. Wang, B. Jia, Y. Deng, X. Wang, Y. Jing, and Y. Li, Commun. Phys. **4,** 1 (2021).

[43] I. Mandal and E. J. Bergholtz, Phys. Rev. Lett. **127,** 186601 (2021).